Structural phase transformations in annealed Pt/Mn/Fe trilayers

To cite this article before publication: Ivan Kruhlov *et al* 2020 *J. Phys.: Condens. Matter* in press https://doi.org/10.1088/1361-648X/ab9269

Structural phase transformations in annealed Pt/Mn/Fe trilayers

I. O. Kruhlov[1], O. V. Shamis[1], N. Y. Schmidt[2], M.V. Karpets[1], S. Gulyas[3,4], E. Hadjixenophontos[5,6], A. P. Burmak[1], S. I. Sidorenko[1], G. L. Katona[3], G. Schmitz[5], M. Albrecht[2], and I. A. Vladymyrskyi[1,*]

[1]Metal Physics Department, National Technical University of Ukraine "Igor Sikorsky Kyiv Polytechnic Institute", Prospect Peremogy 37, 03056 Kyiv, Ukraine

[2]Institute of Physics, University of Augsburg, Universitätsstraße 1, D-86159 Augsburg, Germany

[3]University of Debrecen, Faculty of Science and Technology, Department of Solid State Physics, P.O. Box 400, H-4002 Debrecen, Hungary

[4]University of Debrecen, Doctoral School of Physics, P.O. Box 400, H-4002Debrecen, Hungary

[5]University of Stuttgart, Department of Materials Science, Chair of Materials Physics, Heisenbergstrasse 3, D-70569, Stuttgart, Germany

[6]German Aerospace Center (DLR), Institute of Engineering Thermodynamics, High Temperature Systems and Process Development, Pfaffenwaldring 38-40, D-70569 Stuttgart, Germany

*Corresponding author
(e-mail: vladymyrskyi@kpm.kpi.ua)

Abstract

Thermally-activated phase transitions in Pt/Mn/Fe thin films were investigated by a combination of x-ray diffraction, transmission electron microscopy, secondary neutral mass spectrometry depth profiling, atomic force microscopy, and magnetic properties measurements. Post-annealing was carried out in vacuum to different temperatures up to 620 °C. Initially, at temperatures between 280 °C – 450 °C first $L1_0$-MnPt is formed at the Mn/Pt interface followed by the most likely formation of metastable bcc Fe_3Pt, which gets transformed by further annealing to fcc Fe_3Pt and eventually to chemically ordered $L1_2$-Fe_3Pt. The final product after annealing at 620 °C consists of two interesting phases, which are relevant for spintronic applications, antiferromagnetic $L1_0$-MnPt with addition of Fe and ferromagnetic $L1_2$-Fe_3Pt, consistent with the initial element composition.

Key words: chemical ordering, solid state reactions, magnetic thin films, $L1_0$-MnPt, $L1_0$-FeMnPt, Fe_3Pt

Introduction

Structural phase formation induced by thermally-activated diffusion processes and intermixing of multilayer stacks is a promising reaction pathway for synthesis of novel thin film materials. In particular, the sequence of structural phase transitions in layered structures during annealing could differ from those predicted by corresponding bulk phase diagrams due to sufficient deviation from thermodynamic equilibrium. For instance, thermally-activated diffusion intermixing in Cu/Sn bilayers, which are relevant for nano-electronic applications, can lead to the formation of different metastable phases. Annealing at 100 °C of the Cu(80 nm)/Sn(20 nm) stack leads to formation of the Cu_3Sn phase and following annealing at 200 °C leads to the unexpected formation of the metastable Cu_4Sn phase, which should be formed at temperatures higher than 350 °C, according to the Cu-Sn bulk phase diagram. This phenomenon was explained based on the Ostwald's rule of growth stages, stating that a system being far from equilibrium approaches the equilibrium state with steps, involving the minimum change of the free energy rather than reaching the equilibrium directly [1]. In this regard, various factors such as layer stacking [2-4], annealing conditions [5-7], or substrate choice [8-10] will strongly affect the development of diffusion processes and phase formation.

Numerous theoretical [11-14] and experimental [15-18] studies of diffusion and phase transformations of materials that are of particular interest for applications in spintronics and data storage, are available in the literature. For instance, post-annealing of Pt/Fe bilayers at relatively low-temperatures, which ensure diffusion processes limited to grain boundary mechanisms, could lead to full homogenization of chemical composition throughout the film or even to $L1_0$ chemical ordering [19, 20]. In this process, phase formation occurs via the movement of grain boundaries as a result of grain boundary diffusion, leaving behind an area of reacted product [21]. Furthermore, introduction of additional intermediate layers into Pt/Fe stacks could modify significantly the phase transition temperatures [20, 22-24], the sequence of structural transitions that occur upon annealing [25], or even induce metastable phases [26]. In this regard, Mn is an interesting element to be used as an additional layer in Fe/Pt stacks since it could form various binary and ternary phases in this system and strongly affect the magnetic properties due to antiferromagnetic coupling between Fe and Mn magnetic moments. Early investigations of the bulk FeMnPt phase diagram [27] revealed that in $(Fe_{1-x}Mn_x)Pt$ phases for an intermediate concentration of Mn (x = 0.2 – 0.45) there are two stable phases present – ferromagnetic $L1_0$-FePt and antiferromagnetic $L1_0$-MnPt. However, most of available studies are related to alloyed thin films of the quasi-binary $(Fe_{1-x}Mn_x)_{50}Pt_{50}$ composition [27-33]. As reported by Crisan et al. [34], annealing of FeMnPt films with various Mn content at 500 °C for 1 hour resulted in a multiphase structure: $L1_0$-FePt, $L1_0$-FeMnPt, and a small amount of bcc-Fe. Moreover,

Chiang et al. [35] obtained a graded elemental distribution through the depth of FePt(25 nm)/PtMn(50 nm) films when deposited at 500 °C on MgO(001) followed by post-annealing at 550 °C. However, the evolution of phase formation during annealing of the layer stacks was not addressed.

In this study, the various stages of structural phase formation and composition occurring in Pt/Mn/Fe trilayers upon annealing to different temperatures up to 620 °C were investigated by a combination of various techniques including x-ray diffraction, transmission electron microscopy, and secondary neutral mass spectrometry depth profiling. In addition, magnetic studies were performed in order to get further evidence for the proposed phase transformations.

Experimental details

Pt(15 nm)/Mn(7.5 nm)/Fe(15 nm)/sub. thin films were deposited by dc magnetron sputtering at room temperature on thermally oxidized Si(100) substrates with a 100 nm-thick amorphous SiO_2 layer using individual Fe (99.99%), Pt (99.99%), and Mn (99.95%) targets. The sputtering powers for Pt, Fe, and Mn were 45 W, 98 W, and 91 W, resulting in sputtering rates of 0.47 Å/s, 0.36 Å/s, and 0.2 Å/s, respectively. All depositions were carried out in a BESTEC UHV sputter system (base pressure of $<5\times10^{-6}$ Pa) using an Ar sputter pressure of 0.5 Pa. Sputtering rates were checked by a quartz crystal microbalance before each deposition. In Fig. 1, a cross-section transmission electron microscopy (TEM) image of the as-deposited Pt/Mn/Fe layer stack is shown confirming the layered structure and layer thicknesses of the prepared film. These as-deposited films were annealed in the temperature range of 155-620 °C in vacuum (10^{-3} Pa) with an average heating rate of 0.5 °C/s. The film temperature during annealing was measured directly at the film top surface by K-type thermocouples. After reaching the final film temperature, the sample holder was removed from the heating stage by a specially adapted lever without breaking the vacuum.
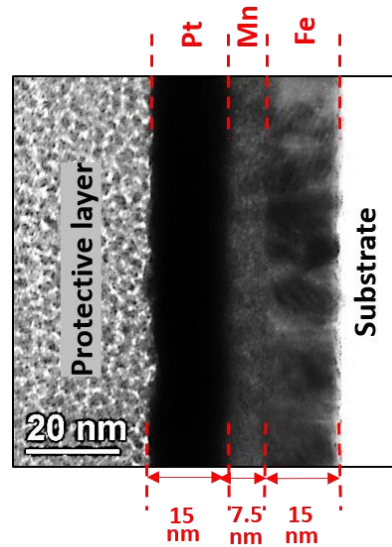
Figure 1. Cross-section TEM image of the as-deposited Pt/Mn/Fe film sample.

The structure and phase composition of the Pt/Mn/Fe film samples after different annealing conditions were analyzed at room temperature by x-ray diffraction (XRD) in (θ-2θ) geometry using a Rigaku Ultima IV diffractometer with Cu-K$_\alpha$ radiation. XRD scans were refined according to Rietveld's full profile approach using the PowderCell 2.4 software [36]. Profiles of diffraction peaks were fitted by a pseudo-Voight function. Quantitative estimation of phase composition was performed taking into account the presence of phase textures according to the March-Dollase model [37]. In this model, the correction of the intensity of any diffraction peak is realized by introducing an effective repetition factor. In case, the investigated phase does not reveal texture, the texture coefficient is equal to 1, and if all grains are oriented in the same direction this coefficient gets zero, while in intermediate cases it takes values between 1 and 0. Since some of the obtained XRD scans show second order harmonic reflection from the Si(400) plane, the angle interval of $32.2\,^\circ$ – $38\,^\circ$ was excluded from Rietveld's analysis. Finally, the following parameters were refined by Rietveld's approach: lattice constants, relative phase abundance, function parameters of diffraction maximums, parameters of sample shift from zero value and coefficient of 7-order polynomial for background description. Weight R-factor (R_{wt}) and expected R-factor (R_{exp}) discrepancy indexes of Rietveld's analysis were calculated using the standard methodology [38]. In addition, the goodness of the Rietveld's fit (χ^2) was estimated as the ratio of (R_{wt}/R_{exp})^2. The profile refinement is considered as perfect when χ^2 is equal to 1, while the goodness decreases for larger values.

Furthermore, secondary neutral mass spectrometry (SNMS, INA-X system, SPECS GmbH) depth profiling was carried out in order to follow the changes in the elemental distribution through the film depth. For the SNMS experiments, Ar plasma was used as a source of bombarding positive ions

as well as a post-ionization medium, while the sputtered area was adjusted to be 3 mm in diameter. The concentration (in at. %) of the elements was determined from the measured intensities, assuming a linear dependence of the intensities on concentration. In addition, cross-sectional TEM imaging of selected samples was performed on a Philipps FEG CM200 system. The thinning of the samples was carried out by focused ion-beam technique with Ga^+ ions and Pt protective coating in a dual beam system (SCIOS, Thermo Fisher Scientific). Energy-dispersive x-ray spectroscopy (EDX) was used during TEM measurements in order to evaluate the chemical composition of different grains of the film. The surface morphology of the samples was analyzed by atomic force microscopy (AFM, Dimension Icon, Bruker GmbH). Magnetic properties of the films were examined using superconducting quantum interference device-vibrating sample magnetometry (SQUID-VSM, MPMS3, LOT-QuantumDesign GmbH). *M-H* hysteresis loops of the as-deposited and post-annealed samples were measured at room temperature in magnetic fields up to ±70 kOe.

Results and discussion

XRD (θ-2θ) scans of the sample series after different post-annealing treatments are summarized in Fig. 2 and 3. Starting with the as-deposited film (Fig. 2a), only reflections originating from face-centered cubic (fcc) Pt and body-centered cubic (bcc) Fe are observed while Mn seems to appear most likely XRD amorphous. Absence of Mn peaks on the XRD patterns could be caused by its fine grain structure consisting of the complex cubic α-Mn phase [39]. The SNMS depth profile of the as-deposited film (Fig. 4a) suggests relatively sharp interfaces of the layer stack, as confirmed by corresponding TEM imaging (Fig. 1).

First notable changes in XRD patterns and elemental distribution through the film depth compared to the as-deposited sample are observed for the sample annealed at 280 °C. As can be seen in the corresponding depth profile (Fig. 4c), intensive intermixing between Mn and Pt layers is present. XRD measurements (Fig. 2c) confirm the formation of the polycrystalline chemically ordered *L1₀*-MnPt phase with pronounced (001), (002), and (110) reflections. Based on the initial layer thicknesses of the as-deposited Pt/Mn/Fe sample, the elemental concentrations in a fully mixed system would give 34 at.% Pt, 21 at.% Mn, and 45 at.% Fe. Thus, Mn and Pt can be almost fully consumed in the *L1₀*-MnPt phase, assuming a maximal Pt content of 60 at.% (according to the phase diagram [40, 41]). In addition, a pronounced Mn segregation towards the film surface was detected by depth profiling. It should be noted that due to the high affinity of Mn to oxygen [29], oxidation of this surface segregation layer is expected [31].

Annealing up to 400 °C did not result in a significant change in crystal structure except of a slight shift of the Fe(110) reflection towards lower 2θ angles (Fig. 2d). This shift could indicate the initial formation of a Fe-rich solid solution with Pt as a result of bcc lattice expansion due to partial substitution of Fe sides by the larger Pt atoms [42].

After further increase of the annealing temperature to 450 °C, the XRD pattern shown in Fig. 2e reveals the appearance of an additional diffraction peak at $2\theta = 43.07°$ which could originate from γ-FeMn(111), a non-coplanar antiferromagnet at room temperature [43] or more likely to the formation of the metastable bcc Fe_3Pt phase [42]. The corresponding SNMS depth profile supports this assumption by the observation of a moderate penetration of Pt and Mn into the Fe layer (Fig. 4f), yet the concentration distribution does not correspond to the equiatomic FeMn phase favoring the presence of bcc Fe_3Pt. However, SNMS profiling has limits as an integral method, giving only average values over a sample area without lateral resolution. Therefore, film roughness will drastically affect and limit the depth resolution. In this regard, AFM imaging was performed on the sample series at room temperature showing a severe increase in route mean square (rms) roughness for samples annealed above 400 °C (Fig. 5). Thus, SNMS data need to be considered with caution as the results at these temperatures are not reliable.

In order to get more information on the present phases occurring for the film annealed at 450 °C, EDX spectra were measured at different locations of the prepared TEM lamella (Fig. 6a,b). Near the surface, a high concentration of Mn and Pt was detected (grains 1 and 2), which is in agreement with depth profiles and XRD results confirming the presence of the $L1_0$-MnPt phase, while the bottom layer close to the substrate (grains 3 and 4) consists mainly of Fe along with Pt and Mn supporting the presence of the Fe_3Pt phase.

With further increase of the annealing temperature up to 500 °C, the XRD intensity of the $L1_0$-MnPt reflections gets more pronounced (Fig. 2f). It is suggested that Fe further diffuses towards the surface and gets incorporated into the $L1_0$ structure. Therefore, it is concluded that a $L1_0$-FeMnPt ternary alloy is formed, which remains antiferromagnetic due to the low Fe content. Interestingly, the bcc Fe_3Pt reflection has almost vanished but shifted to lower angles (at $2\theta \approx 41.9°$, Fig. 1f) indicating the transition to the fcc Fe_3Pt structure which transforms into chemically ordered $L1_2$-Fe_3Pt upon further annealing. Please note that the (111) reflections of the two Fe_3Pt structures, fcc and $L1_2$, are almost identical, but it is expected that beyond 500 °C the chemically ordered phase is more favored [42]. Temperature increase above 500 °C leads to a broadening of the (111) peak of the $L1_0$-FeMnPt phase and to a pronounced intensity enhancement of the (111) reflection of the Fe_3Pt phase, indicating changes of the texture parameters and grain size of these phases under temperature increase.

The presence of these two phases is consistent with the initial elemental composition of 34 at.% Pt, 21 at.% Mn, and 45 at.% Fe. Assuming that all Mn is consumed in the equiatomic $L1_0$-MnPt phase with a slight amount of Fe and some Mn at the surface, the remaining Pt and Fe have a ratio of about 1:3 resulting in the $L1_2$-Fe₃Pt phase.
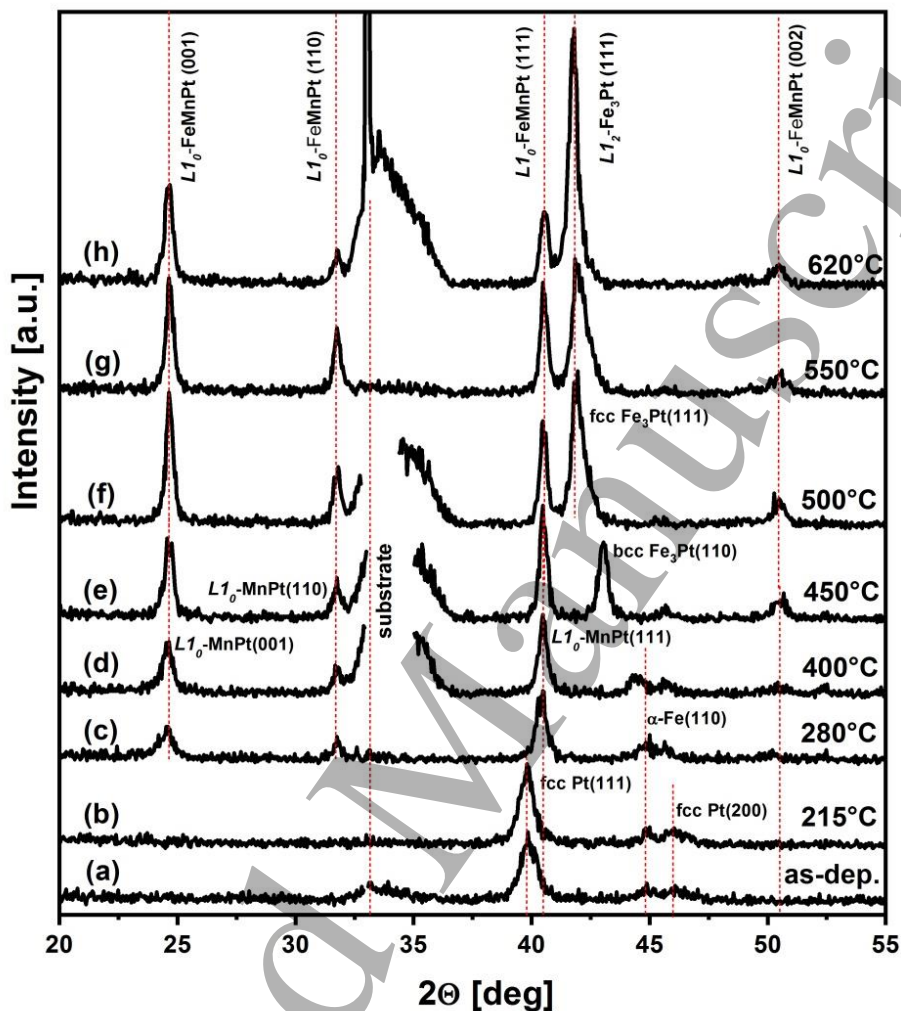

Figure 2. *(a-h) XRD ($\theta - 2\theta$) scans of Pt(15 nm)/Mn(7.5 nm)/Fe(15 nm) films after deposition and post-annealing at different temperatures.*
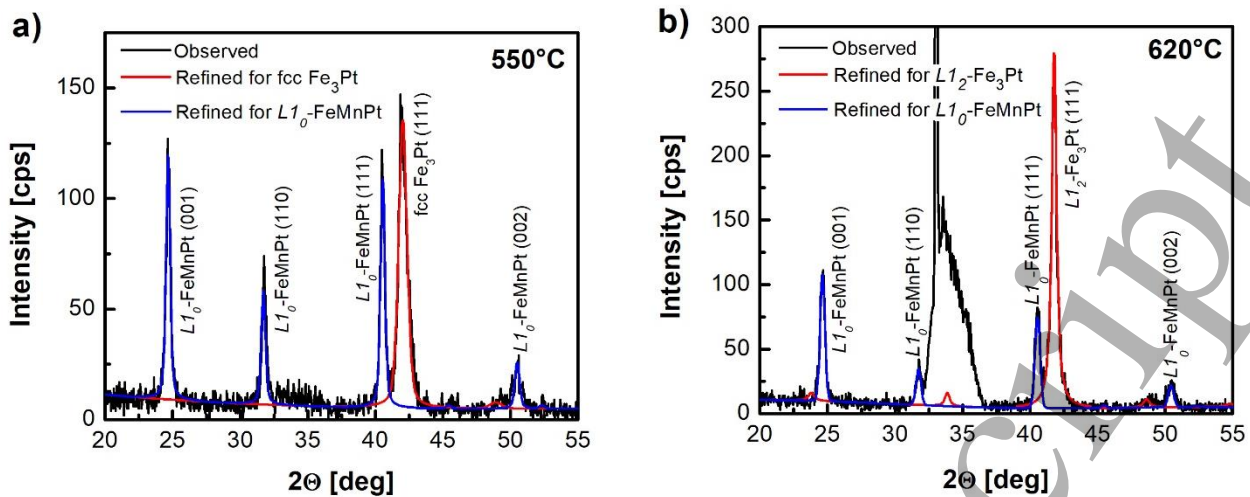
7

Figure 3. XRD patterns of Pt(15 nm)/Mn(7.5 nm)/Fe(15 nm) films post-annealed at 550 °C (a) and 620 °C (b). In addition, the refined diffractograms applying Rietveld's analysis are included. In case of (b) the angle interval of 32.2 – 38 degrees was excluded from refinement.

Application of Rietveld's full profile fitting allowed to refine the lattice parameters (a and c), relative concentrations (in mass %), and the texture coefficients of different phases formed after various heat treatment stages. The results are summarized in table 1 giving the relevant parameters of the samples after various heat treatment stages. As an example, diffractograms including refined patterns of films annealed at 550 °C and 620 °C are shown in Fig. 3a and b, respectively.

The estimation of relative phase concentrations was performed for films annealed above 400 °C, where the coexistence of different phases became substantial. The evolution of Fe_3Pt phases with different crystal lattices starting from bcc Fe_3Pt (450 °C) to $L1_2$-Fe_3Pt (620 °C) caused a reduction of the $L1_0$-FeMnPt amount from 65 to 55 mass.%, respectively. According to the XRD refined data, the final product consists of 55 mass.% of $L1_0$-FeMnPt and 45 mass.% of $L1_2$-Fe_3Pt phases. Furthermore, the presence of preferential grain orientation was investigated by analyzing the texture coefficients τ. A tendency of increment in number of grains with {001} orientation was detected for the $L1_0$-(Fe)MnPt tetragonal phase, which reflected in the decrease of $\tau001$ values with increasing the heat treatment temperature up to 500 °C. The following increase of treatment temperature does not lead to sufficient changes in texture parameter. Simultaneously, dominant {111} texture was revealed in both Fe_3Pt cubic phases starting from 500 °C. Moreover, a subsequent decrease of the lattice constants of the $L1_0$-FeMnPt phase upon annealing above 450°C was obtained which is additionally supporting the hypothesis of Fe incorporation into the already formed $L1_0$-MnPt ordered structure.

Table 1. Evolution of structural properties – a and c lattice constants (Å), relative concentration (M in mass %), texture coefficients (τ) – of phases formed after various heat treatment

stages (values in brackets provide absolute errors). In addition, the Rietveld's refinement discrepancy indexes (weight R-factor (R_{wt}), expected R-factor (R_{exp}), χ^2) are given.

Phase		as-dep.	215 °C	280 °C	400 °C	450 °C	500 °C	550 °C	620 °C
Pt	a	3.920(7)	3.930(5)						
α-Fe	a	2.859(9)	2.859(8)	2.867(7)	2.886(7)				
$L1_0$-MnPt	a			2.829(4)	2.826(3)				
	c			3.644(6)	3.634(3)				
	τ_{001}			0.79	0.71				
$L1_0$-FeMnPt	a					2.831(3)	2.830(3)	2.827(2)	2.825(3)
	c					3.625(4)	3.620(4)	3.619(3)	3.624(4)
	τ_{001}					0.68	0.60	0.67	0.65
	M					65(7)	52(6)	51(6)	55(6)
bcc Fe$_3$Pt	a					2.977(5)			
	M					35(7)			
fcc Fe$_3$Pt	a						3.734(6)	3.727(5)	
	τ_{111}						0.45	0.46	
	M						48(6)	49(6)	
$L1_2$-Fe$_3$Pt	a								3.750(6)
	τ_{111}								0.35
	M								45(6)
	R_{wp}	4.7	3.9	3.8	6.4	6.2	6.1	4.2	6.7
	R_{exp}	4.3	3.8	3.7	2.8	2.5	2.4	3.2	2.5
	χ^2	1.195	1.053	1.055	5.225	6.15	6.46	1.72	7.18

The estimated values of the χ^2 parameter are close to 1 for the as-deposited film and samples post-annealed at 215 °C, 280 °C, and 550 °C, suggesting very high accuracy of Rietveld's refinement. For the other samples the χ^2 parameter is larger than 1 but still suggesting reasonable correctness of the Rietveld's fitting. The difference is mainly caused by the presence or absence of the Si(400) reflection on the observed XRD patterns.

To summarize, from the structural and chemical analysis based on XRD, SNMS, and TEM results, the following sequence of the main phase transformations with annealing temperature can be proposed: Pt/Mn/Fe $\xrightarrow{280\,°C}$ $L1_0$-MnPt + α-Fe $\xrightarrow{450\,°C}$ $L1_0$-FeMnPt+ bcc Fe$_3$Pt $\xrightarrow{500\,°C}$ $L1_0$-FeMnPt+ fcc Fe$_3$Pt $\xrightarrow{620\,°C}$ $L1_0$-FeMnPt+ $L1_2$-Fe$_3$Pt.
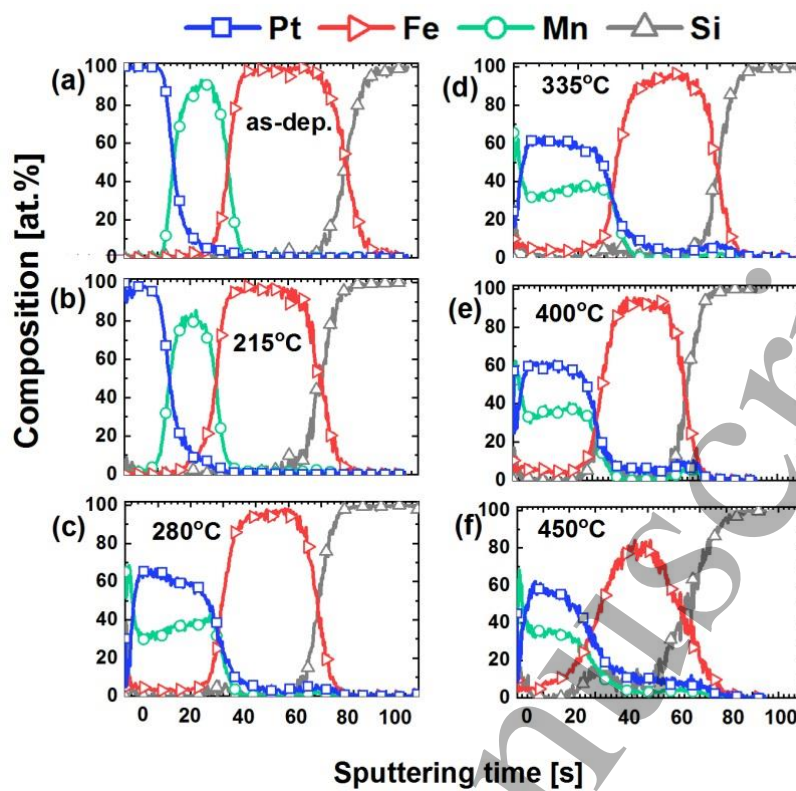
Figure 4. *(a-h) SNMS composition-depth profiles of Pt/Mn/Fe films after deposition and post-annealing at different temperatures.*
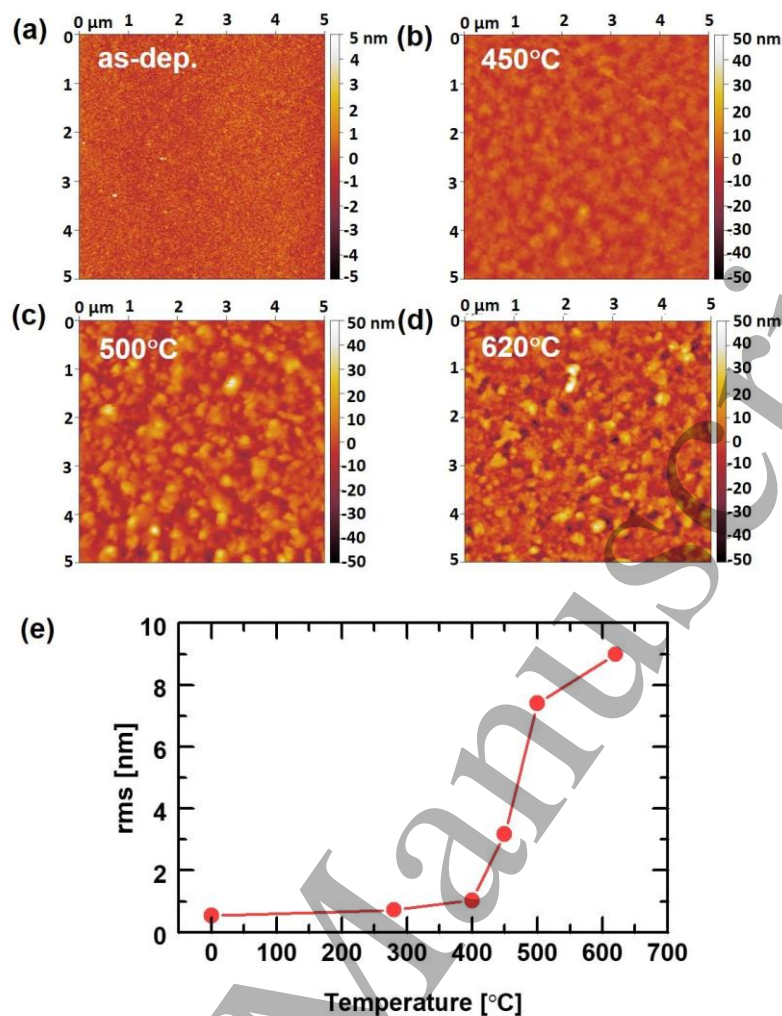
***Figure* 5.** *AFM images of the (a) as-deposited and (b-d) annealed Pt/Mn/Fe film samples taken at room temperature. (e) Corresponding rms roughness in as-deposited state ("0 °C") and after annealing at different temperatures.*
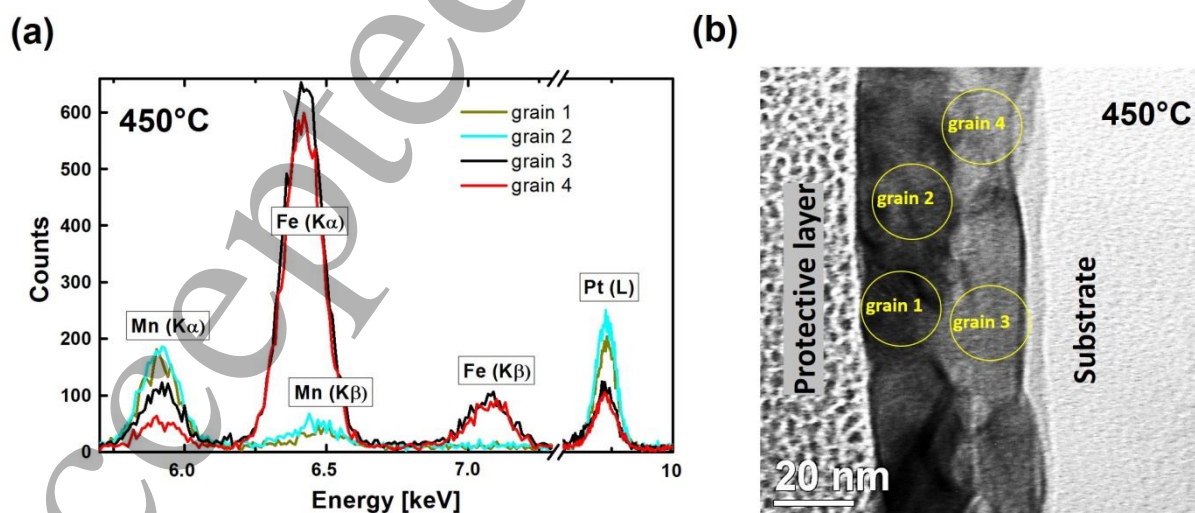

***Figure* 6.** *(a) EDX spectra and (b) corresponding cross-section TEM image of a 450 °C post-annealed sample. EDX spectra were taken at specific locations of the TEM lamella as marked in (b).*

11

Magnetic studies are very useful in order to get further evidence for the proposed phase transformations. Therefore, magnetic M-H hysteresis loops in in-plane and out-of-plane geometry (Fig. 7a-e) were measured at room temperature to extract the in-plane coercivity H_c (Fig. 7f) and saturation magnetization M_s (Fig. 7h). For the latter, only the volume of the full initial layer stack was considered. Therefore, the M_s values reveal only relative changes upon phase formation and cannot be compared to material specific M_s values. All films clearly show an easy axis of magnetization in the film plane. As expected, no pronounced change in magnetic properties for samples annealed up to 400 °C were observed, indicating a rather unaffected Fe layer with an in-plane easy axis of magnetization due to magnetic shape anisotropy. Above 400 °C, there is a continuous decrease in magnetization, which indicates the incorporation of Fe into the $L1_0$-MnPt lattice, compensating the magnetic moment of Fe. Please note the additionally formed bcc Fe_3Pt phase is expected to be ferromagnetic at room temperature exhibiting a rather high M_s value (1530 emu/cm^3, [42]), thus this phase cannot be the origin of the reduction in magnetization. However, the maximum in coercivity at 450 °C might be related to strong domain wall pinning effects at the bcc Fe_3Pt grain boundaries and increased magnetic anisotropy. Furthermore, the structural transition of bcc Fe_3Pt into fcc Fe_3Pt, which is expected to be in a paramagnetic state at room temperature [44], explains the lowering in coercivity and in magnetization which reveals a minimum after annealing at 500 °C, the temperature where fcc Fe_3Pt is dominantly formed. The residual magnetization might be due to some Fe remains and onset of $L1_2$-Fe_3Pt formation. Further rise of annealing temperature up to 620 °C results in the favored development of ferromagnetic $L1_2$-Fe_3Pt phase with rather high Ms value (1270 emu/cm^3 [42]) accompanied by the evolution of antiferromagnetic $L1_0$-FeMnPt phase and changes of its phase content, together causing a strong increase in saturation magnetization. It should be pointed out, that since all mentioned phase transitions are not sharp and the coexistence of phases with different magnetic properties is present, the magnetization from each phase cannot be extracted from the total magnetization of the stack. Thus, the interpretation of temperature dependence of magnetic properties should only be accompanied with the results from the structural and chemical measurements.

In order to provide additional evidence for the presence of a paramagnetic fcc Fe_3Pt phase, the saturation magnetization was analyzed in dependence of the temperature for three samples post-annealed to 450 °C, 500 °C, and 550 °C (Fig. 7g). While the sample prepared at 450 °C containing only ferro- and antiferromagnetic phases showed almost no temperature dependence, the other two samples revealed a pronounce increase at lower temperatures which hint to paramagnetic contributions complemented with a broad distribution of magnetic ordering temperatures. However, due to the magnetic background signal of the substrate, which is difficult to subtract, unequivocal conclusion cannot be made.
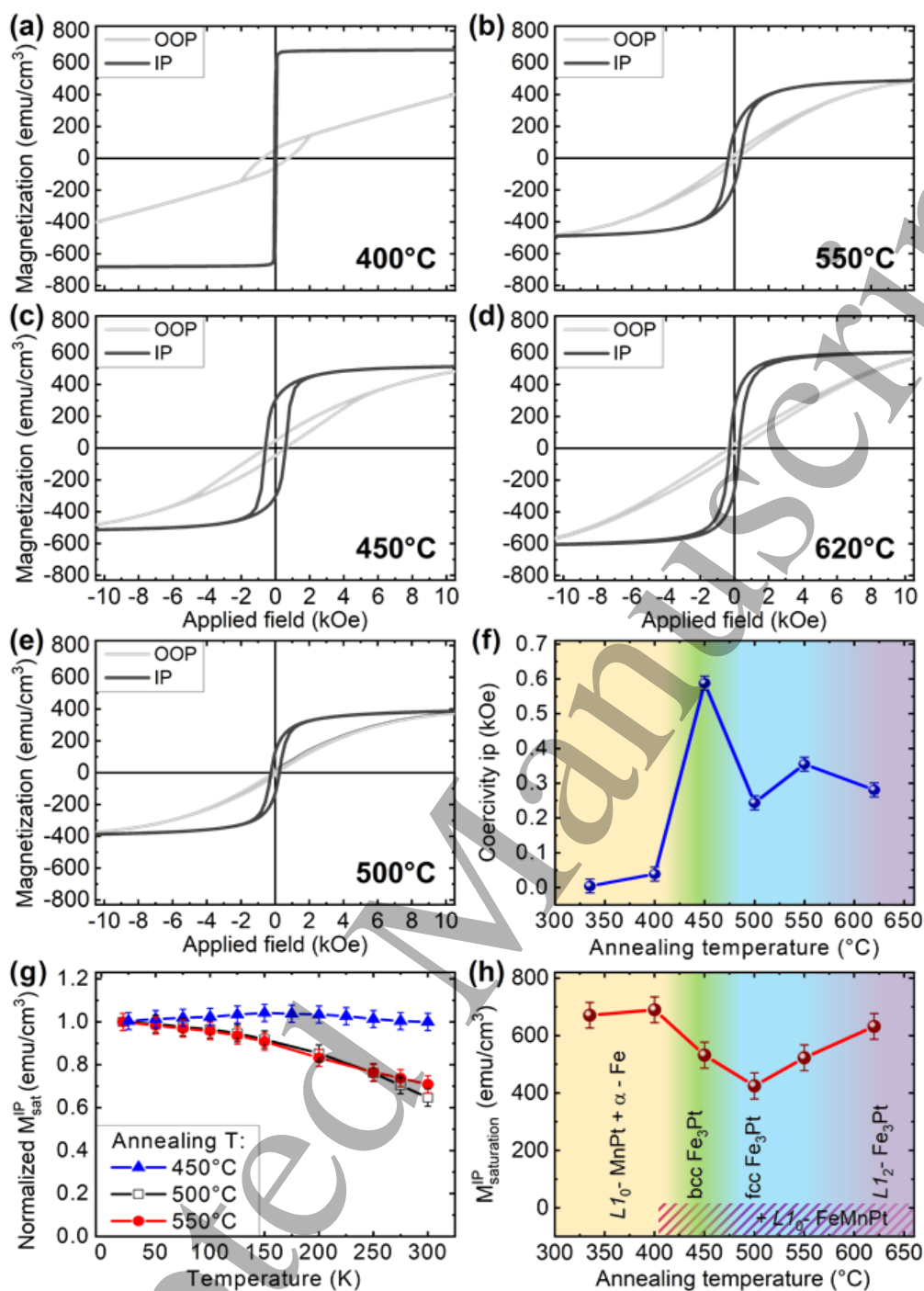
Figure 7. *(a-e) In-plane and out-of-plane M-H hysteresis loops of Pt/Mn/Fe films after deposition and post-annealing at different temperatures. (f) Coercivity (from in-plane loops) and (h) saturation magnetization at room temperature as function of annealing temperature. (g) Normalized saturation magnetization as function of temperature for three samples post-annealed at different temperatures.*

13

Conclusion

The sequence of phase transitions occurring in Pt/Mn/Fe trilayers during post-annealing in vacuum up to 620 °C was investigated. After annealing at 280 °C the ordered binary $L1_0$-MnPt phase was formed and pronounced Mn surface segregation was registered. An unreacted Fe layer remains in the film at these temperatures, dominating the materials magnetic properties. The following increase of the sample temperature up to 450 °C results in the incorporation of Fe to the $L1_0$-MnPt structure and the additional formation of metastable bcc Fe_3Pt. Upon further annealing to 500 °C, the bcc Fe_3Pt structure transforms into the paramagnetic fcc Fe_3Pt structure resulting in a decrease of the saturation magnetization. The following rise in saturation magnetization obtained after annealing at 620 °C is related to the chemical $L1_2$ ordering of Fe_3Pt, which is ferromagnetic at room temperature. The final phase products of $L1_0$-FeMnPt and $L1_2$-Fe_3Pt are consistent with the initial elemental concentrations of the Pt/Mn/Fe trilayer, though the path of synthesis was rather unexpected.

Acknowledgment

References

[1] Oleshkevych A., Zamani A., Kotenko I., Voloshko S., Sidorenko S., and Rennie A.R. 2012 *J. Alloys Cmpd.* **535** 108.

[2] Aboulfadl H., Gallino I., Busch R., and Mucklich F. 2016 *J. Appl. Phys.* **120** 195306.

[3] Srivastava A.K., Yu-Zhang K., Kilian L., Frigerio J.M., and Rivory J. 2007 *J. Mater. Sci.* **42** 185.

[4] Rothhaar U., Oechsner H., Scheib M., and Müller R. 2000 *Phys. Rev. B* **61** 974.

[5] Li J., Sha N., and Zhao Z. 2018 *Appl. Surf. Sci.* **454** 233.

[6] Hu B., Xu J., Wang J., Liu B., and Du B. 2018 *Mater. Lett.* **232** 51.

[7] Yao J., Zheng X., Cai W., and Sui J. 2017 *J. Alloys Cmpd.* **695** 1243.

[8] Desai N.D., Ghanwat B., Khot K.V., Mali S.S., Hong C.K., and Bhosale P.N. 2016 *J. Mater. Sci. - Mater. Electron.* **27** 2385.

[9] Su L., Yu Y., Cao L., and Zhang Y. 2015 *Nano Res.* **8** 2686.

[10] Oujja M., Martin-Garcia L., Rebollar E., Quesada A., Garcia M.A., Fernandez J.F., Marco J.F., Figuera J., and Castillejo M. 2018 *Appl. Surf. Sci.* **452** 19.

[11] Kim B.-H., Chung Y.-C. 2009 *J. Appl. Phys.* **106** 044304.

[12] Toinin J.P., Hoummada K., Bertoglio M., and Portavoce A. 2016 *Scr. Mater.* **122** 22.

[13] Mohammadzadeh R., and Mohammadzadeh M.2018 *J. Appl. Phys.* **124** 035102.

[14] Feng Y., Liu M., Shi Y., Ma H., Li D., Li Y., Lu L., and Chen X. 2019 *Prog. Nat. Sci.* **29** 341.

[15] Panda R., Naik R., and Mishra N.C. 2019 *J. Alloys Compd.* **778** 819.

[16] Chakravarty S., Chirayath V.A., Gangavarapu A., Parida P., and Dasgupta A. 2015 *J. Phys. D: Appl. Phys.* **48** 305303.

[17] Pontes F.M., Pontes D.S.L., Leite E.R., Longo E., Chiquito A.J., Machado M.A.C., Pizani P.S., and Varela J.A. 2004 *Appl. Phys. A* **78** 349.

[18] Peng Y., Wang F., Wang Z., Alsayed A.M., Zhang Z., Yodh A.G., and Han Y. 2015 *Nat. Mater.* **14** 101.

[19] Katona G.L., Vladymyrskyi I.A., Makogon I.M., Sidorenko S.I., Kristaly F., Daroczi L., Csik A., Liebig A., Beddies G., Albrecht M., and Beke D.L. 2014 *Appl. Phys. A* **115** 203.

[20] Vladymyrskyi I.A., Gafarov A.E., Burmak A.P., Sidorenko S.I., Katona G.L., Safonova N.Y., Ganss F., Beddies G., Albrecht M., and Makogon Y.N. 2015 *J. Phys. D: Appl. Phys.* **49** 035003.

[21] Beke D.L., Kaganovskii Y., Katona G.L. 2018 *Prog. Mater. Sci.* **98** 625.

[22] Pavlova O.P., Verbitska T.I., Vladymyrskyi I.A., Sidorenko S.I., Katona G.L., Beke D.L., Beddies G., Albrecht M., and Makogon I.M. 2013 *Appl. Surf. Sci.* **266** 100.

[23] Yu S.Y., Li H.-B., Li W.L., Liu M., and Fei W.D. 2008 *J. Magn. Magn. Mater.* **320** L125.

[24] Wu Y.-C., Wang L.-W., and Lai C.-H.2007 *Appl. Phys. Lett.* **91** 072502.

[25] Gupta R., Medwai R., Sharma P., Mahapatro A.K. Annapoorni S. 2013 *Superlattices Microstruct.* **64** 408.

[26] Katona G.L., Safonova N.Y., Ganss F., Mitin D., Vladymyrskyi I.A., Sidorenko S.I., Makogon Iu.N., Beddies G., Albrecht M. and Beke D.L. 2015 *J. Phys. D: Appl. Phys.* **48** 175001.

[27] Menshikov A.Z., Antropov V.P., Gasnikova G.P., Dorofeyev Y.A., and Kazantsev V.A. 1987 *J. Magn. Magn. Mater.* **65** 159.

[28] Xu D.B., Chen J.S., Zhou T.J., and Chow G.M. 2011 *J. Appl. Phys.* **109** 07B747.

[29] Lai C.H. and Ho C.H. 2005 *J. Appl. Phys.* **97** 10J314.

[30] Huang J.C.A., Chang Y.C., Yu C.C., Yao Y.D., Hu Y.M., and Fu C.M. 2003 *J. Appl. Phys.* **93** 8173.

[31] Safonova N.Y., Riepp M., Klein O., and Albrecht M. 2017 *J. Phys. Conf. Ser.* **903** 12023.

[32] Meyer G. and Thiele J.-U. 2006 *Phys. Rev. B* **73** 214438.

[33] Manoharan E.A., Mankey., Hong Y.-K. 2017 *J. Magn. Magn. Mater.* **438** 111.

[34] Crisan O., Vasiliu F., Crisan A.D., Mercioniu I., Schinteie G., and Leca A. 2019 *Mater. Charact.* **152** 245.

[35] Chiang C.C., Tsai W.C., Wang L.W., Hou H.C., Liao J.W., Lin H.J., Chang F.H., Kirby B.J., and Lai C.H. 2011 *Appl. Phys. Lett.* **99** 212504.

[36] Kraus W. and Nolze G. 1996 *J. Appl. Crystallogr.* **29** 301.

[37] Dollase W.A. 1986 *J. Appl. Crystallogr.* **19** 267.

[38] Toby B.H. 2006 *Powder Diffr.* **21** 67.

[39] Andrieu S., Fischer H.M., Traverse A., Piecuch M. 1997 *J. Magn. Magn. Mat.* **165** 185.

[40] Raub E. and Mahler W. 1955 *Z. Metallkd.* **46** 282.

[41] Ladwig P.F., Chang Y.A., Linville E.S., Morrone A., Gao J., Pant B.B., Schlutz A.E., and Mao S. 2003 *J. Appl. Phys.* **94** 979.

[42] Hsiao S.N., Chen S.K., Liu S.H., and Lee H.Y 2012 *J. Appl. Phys.* **111** 07A313.

[43] Shiomi Y. 2018 *AIP Advances* **8** 085018.

[44] Mizoguchi T., Akimitsu M., and Chikazumi S. 1973 *J. Phys. Soc. Jpn.* **34** 932.